ALLEVIATION OF ROTOR VIBRATIONS INDUCED BY DYNAMIC STALL USING ACTIVELY CONTROLLED FLAPS WITH FREEPLAY

Gilles Depailler [i] and Peretz P. Friedmann [ii]
Department of Aerospace Engineering
University of Michigan, Ann Arbor, Michigan

Abstract

This paper presents a successful treatment of the helicopter vibration reduction problem at high advance ratios, taking into account the effects of dynamic stall. The ONERA model is used to describe the loads during stall, in conjunction with a rational function approximation for unsteady loads for attached flow. This study represents the first successful implementation of vibration reduction in presence of dynamic stall, using single and dual trailing edge flap confogurations. A physical explanation for the vibration reduction process is also provided. Saturation limits on the control deflections are imposed, which limit flap deflections to a practical range. Effective vibration reduction is achieved even when imposing practical saturation limits on the controller. Finally, the robustness of the vibration reduction process in the presence of a freeplay type of nonlinearity is also demonstrated.

Notation

a, a_0, a_2	Separated flow empirical coefficients
b	Blade semi chord
C_{d0}	Blade drag coefficient in attached flow
c_b	Blade chord
c_{cs}	Flap chord
c_{wu}	Multiplier for W_u weighting matrix
D	Drag force per unit span
$D_0,\ D_1$	Generalized flap motions
$\mathbf{d}$	Generalized force vector
E, E_2	Separated flow empirical coefficients
fC_{df}	Equivalent flat plate fuselage area
h	Plunge displacement at the elastic axis
$\mathbf{h}$	Generalized motion vector
H_m	Hinge moment around flap hinge
J	Objective function
J_R	Sum of the squares of the trim residuals
K_δ	Spring constant for the freeplay nonlinearity model
L	Lift force per unit span
L_{cs}	Control surface length
M	Mach number
M_{AC}	Pitch moment per unit span hub moments
N_b	Number of blades
p_0, p_1, p_c, p_h	Functions of M
$\mathbf{q_b}$	Vector of blade degrees of freedom
$q_{wi}, q_{vi}, q_{\phi i}$	Participation coefficients in the flap/lead-lag/torsional mode shape
r	Coordinate along the length of the blade
r, r_0, r_2	Separated flow empirical coefficients
s_l	Function of M derived from flat plate theory
s_m, s_d	Empirical functions of M
t	Time
t_0	Time when $\alpha = \alpha_{cr}$
$\mathbf{T}$	Transfer matrix
$\mathbf{u_i}$	amplitudes of control input harmonics

[i] Ph. D. Candidate
[ii] François-Xavier Bagnoud Professor

U	Air velocity relative to the blade section
	value
W_0, W_1	Generalized airfoil motions
$\mathbf{W_z}$, $\mathbf{W_u}$	Weighting matrices
x_{cs}	Control surface position
X_{FA}, Z_{FA}	Longitudinal and vertical offsets between rotor hub and helicopter aerodynamic center
X_{FC}, Z_{FC}	Longitudinal and vertical offsets between rotor hub and helicopter center of gravity
$\mathbf{z_i}$	amplitudes of vibratory load harmonics
α	Blade angle of attack
α_{cr}	Critical angle of attack for dynamic stall onset
α_f, α_s	Functions of M
α_R	Rotor shaft angle
γ	Lock number
δ_a	Freeplay angle
δ_e	Torsion angle seen by the spring modeling the actuator
δ_f	Flap deflection
δ_p	Presribed flap deflection, degrees, given by the control vector $\mathbf{u}$
Γ_1, Γ_2	Aerodynamic separated flow states
ΔC_L	Measure of stall
Δt	Stall time delay
$\theta_0, \theta_{1s}, \theta_{1c}$	Collective and cyclic pitch angles
θ_{pt}	Pretwist angle
θ_t	Tail rotor constant pitch
κ_l	Function of M derived from flat plate theory
$\kappa_m, \kappa_d, \lambda$	Empirical functions of M
μ	Advance ratio
ϕ_R	Lateral roll angle
ψ	Azimuth angle
Ω	Rotor angular velocity
ω_{F1}, ω_{L1}, ω_{T1}	Rotating fundamental blade frequencies in flap, lead-lag and torsion, respectively, nondimensionalized with respect to Ω.
$\dot{(\,)}$	Derivatives with respect to time

Subscripts

A	Aerodynamic
d	coefficient connected to drag
G	Gravitational
I	Inertial
j	Represents l, m or d
l	coefficient connected to lift
m	coefficient connected to moment
S	coefficient in separated flow

Introduction and Background

One of the primary concerns in rotorcraft design is the issue of vibrations and its reduction. High levels of vibration may lead to passenger discomfort, fatigue of helicopter components and increased noise. These phenomena decrease rotorcraft performance and increase cost. Thus, the issues of vibration prediction and its reduction to the lowest possible levels are of primary importance to the helicopter designer.

The largest contributor to vibrations in a helicopter is the rotor. The rotor blades transfer vibratory loads from the hub to the fuselage at harmonics that are predominantly N_b/rev. The first methods devised for vibration reduction were passive, and were based on vibration absorbers and isolators. Later, active nethods have been implemented. In recent years, actively controlled trailing edge flaps have been investigated as a means for vibration control in helicopter rotors [1–5]. Experimental results from wind tunnels using the ACF were also presented by Straub [6]. Other vibration reduction studies using the ACF were also conducted [7, 8]. Additional information on vibration reduction using the ACF can be found in a recent survey paper [9].

Active control strategies have been developed that can reduce vibration levels well below those achieved through traditional passive methods such as dampers and mass tuning [1]. Among the active control approaches, two fundamentally different strategies have emerged: higher harmonic control (HHC) and individual blade control (IBC). Three approaches have been used for individual blade control: actuation at the blade root [1], the actively controlled flap (ACF) [2–4], and active twist rotor blades [10, 11]. Vibrations are controlled at their source, on the rotor blades, by manipulating the unsteady aerodynamic loading in the rotating system.

Dynamic stall is a phenomenon that affects helicopter performance at high advance ratios, and the vibrations induced by dynamic stall limit helicopter performance at high speeds. A good description of the dynamic stall phenomenon is provided in Chapter 9 of Ref. 12. The main effects of dynamic stall

are : (1) a a hysteretic dynamic lift coefficient that is much higher than the corresponding static value, accompanied by (2) large pitching moments; and (3) large increases in the pitch-link vibratory loads that manifest themselves in the pilot's stick and negatively affect controllability. The specific problems of reducing vibrations due to dynamic stall has been studied by Nguyen [13] using HHC, and only a very small amount of vibration reduction was achieved.

Among the available models [12] of dynamic stall, two semi-empirical models have become quite popular and are often used for computational modeling of rotorcraft vibration. These are the ONERA model [14], and the Leishman-Beddoes model [15].

Recently, Myrtle and Friedmann [3] developed a new compressible unsteady aerodynamic model for the analysis of a rotor blade with actively controlled flaps. This model is based on rational function approximation (RFA) of aerodynamic loads, and it has been shown that it produces good accuracy in aeroelastic simulations. De Terlizzi and Friedmann [4] included a nonuniform inflow distribution calculation, based on a free wake model, in the analysis, and simulated vibration reduction at high speeds as well as alleviation of blade vortex interaction (BVI) at low advance ratios.

Valuable experimental results on the practical implementation of the ACF and its application to vibration reduction in the open loop mode, on a Mach-scaled two bladed rotor, were obtained by Fulton and Ormiston [16]. These results were compared with the simulation described in Refs. 4 and 17 and the correlation with the experimental data was found to be quite good, in most cases.

Another problem encountered when using actively controlled flaps for vibration reduction is to account for the drag increase due to flap deflections. Based on this limited information a methodology for accounting for the flap increase due to flap deflections was developed in Ref. 18.

Some practical aspects of control surface behavior, such as freeplay or slack in the linkages associated with the actuation mechanism are often modeled by a freeplay type of nonlinearity. To model the freeplay type of nonlinearity, the model used in Ref. 19, depicted on Figs. 1 and 2, is used. This model has been used in several studies involving freeplay type of nonlinearity [19,20]. Such a freeplay type of nonlinearity is useful for examining the robustness of the vibration reduction scheme under practical conditions.

This paper has several objectives: (1) Development of an improved rotor aerodynamic model by incorporating dynamic stall in the aeroelastic simulation of rotor vibratory loads in forward flight; (2) application of the simulation capability to the vibration reduction problem; and (3) a study of the robustness of vibration alleviation in presence of freeplay type of nonlinearity. This paper represents an important contribution toward the improved fundamental understanding of vibration modeling and its reduction using the ACF under dynamic stall and freeplay conditions.

Aeroelastic Response Model

Structural Dynamic Model. The structural dynamic model is directly taken from [2]. The rotor is assumed to be composed of four identical blades, connected to a fixed hub, and it is operating at a constant angular velocity Ω. The hingeless blade is modeled by an elastic beam cantilevered at an offset e from the axis of rotation, as shown in Figure 3. The blade has fully coupled flap, lead-lag, and torsional dynamics. The strains within the blade are assumed to be small and the deflections to be moderate. The inertia loads are obtained from D'Alembert's principle and an ordering scheme is used to simplify the equations.

The control surfaces are assumed to be an integral part of the blade, attached at a number of spanwise stations. It is assumed that the control surfaces do not modify the structural properties of the blade, only the inertia and aerodynamic loads due to the flaps are accounted for. The control surface is constrained to pure rotation in the plane of the blade cross-section, see Fig. 3.

Tang and Dowell [19] modeled freeplay nonlinearity by changing the torsional stiffness at the hinge of the control surface. This model was also used in Ref. 20. A commonly used representation combines freeplay with a linear torsional spring is shown in Fig. 1 and its force-deflection characteristics are shown in Fig. 2. This freeplay model is combined with the actively controlled flap by enforcing hinge moment equilibrium at the flap hinge. Thus, the flap can be considered as a free flap, provided that an extra restoring moment is added to the hinge moment equilibrium equation. For $|\delta_f - \delta_p| \leq \delta_a$, the spring constant is set to zero, and for $|\delta_f - \delta_p| \geq \delta_a$, it is set to a finite value K_δ. The detailed mathematical formulation of the model modification due to freeplay is presented in a subsequent section.

Aerodynamic Model For Attached Flow. Blade section aerodynamic loads are calculated using RFA, an approach described by Myrtle and Friedmann [3]. The RFA approach is an unsteady time-domain aerodynamic theory that accounts for com-

pressibility, variations in the incoming flow and a combined blade, trailing edge flap configuration in the cross-section. These attributes make the RFA model particularly useful when studying vibration reduction in the presence of dynamic stall. The RFA approach generates approximate transfer functions between the generalized motion vector and the generalized attached flow force vector.

A non-uniform inflow distribution, obtained from a free wake model is employed. The free wake model has been extracted [17] from the rotorcraft analysis tool CAMRAD/JA [21]. The wake vorticity is created in the flow field as the blade rotates, and then convected with the local velocity of the fluid. The local velocity of the fluid consists of the free stream velocity, and the wake self-induced velocity. The wake geometry calculation proceeds as follows: (1) the position of the blade generating the wake element is calculated, this is the point at which the wake vorticity is created; (2) the undistorted wake geometry is computed as wake elements are convected downstream from the rotor by the free stream velocity; (3) distortion of wake due to the wake self-induced velocity is computed and added to the undistorted geometry, to obtain a free wake geometry. The wake calculation model [21] is based on a vortex-lattice approximation for the wake.

An approximate methodology for introducing drag corrections due to flap deflections has been described in Ref. 18. The model for drag corrections for partial span trailing edge flaps used in the attached flow domain combines elements of Refs. 22 and 23. It is given by the following relation:

$$C_{d0} = 0.01 + 0.001225|\delta_f| \tag{1}$$

By contrast, the model used in [2] ("without correction") is:

$$C_{d0} = 0.01 \tag{2}$$

In the baseline (uncontrolled) configuration, the flap is not deflected. In that case, the drag correction is zero.

Aerodynamic Model For Separated Flow. Two families of semi-empirical models that are extensively used and reasonably well documented were described and compared in Ref. 24. In this paper, the ONERA model as modified and presented by Petot [14] is used. The airfoil velocity is expressed using the generalized motions W_0, W_1 shown in Fig. 4 and defined by:

$$W_0 = U\alpha + \dot{h}, \quad W_1 = b\dot{\alpha} \tag{3}$$

The model establishes a transfer function between the generalized motion vector $\mathbf{d} = [W_0, W_1, D_0, D_1]$ and the generalized force vector $\mathbf{h} = [L, M_{AC}, D]$. It is based on linear, time-varying coeffient differential equations: a first-order equation for attached flow

$$\begin{aligned}\dot{\Gamma_1} + \lambda\frac{U}{b}\Gamma_1 &= \lambda\frac{U}{b}p_0 W_0 + \lambda\frac{U}{b}W_1 + \alpha_s p_0 \dot{W_0} \\ &\quad + \alpha_s \sigma \dot{W_1}, \end{aligned} \tag{4}$$

where $\lambda, \alpha_s, p_0, \sigma$ are functions of M derived from flat plate theory, and three second-order ones for separated flow:

$$\begin{aligned}\ddot{\Gamma_{j2}} + a_j.\frac{U}{b}\dot{\Gamma_{j2}} + r_j(\frac{U}{b})^2\Gamma_{j2} &= -[r_j(\frac{U}{b})^2 V \Delta C_L \\ &\quad + E_j.\frac{U}{b}\dot{W_0}, \end{aligned} \tag{5}$$

where $j = l, m, d$. The loads are derived from these expressions

$$L_S = \frac{1}{2}\rho c_b(s_l b\dot{W_0} + \kappa_l b\dot{W_1} + U(\Gamma_{l1} + \Gamma_{l2}) \tag{6}$$

$$M_{AC_S} = \frac{1}{2}\rho c_b^2(s_m b\dot{W_0} + \kappa_m b\dot{W_1} + U(\Gamma_{m1} + \Gamma_{m2}) \tag{7}$$

$$D_S = \frac{1}{2}\rho c_b(s_d b\dot{W_0} + \kappa_d b\dot{W_1} + U(\Gamma_{d1} + \Gamma_{d2}) \tag{8}$$

The attached flow loads in the ONERA model have been modified by Peters [25] to be consistent with Greenberg's unsteady aerodynamic theory. Other features of the ONERA dynamic stall model include the presence of a time delay for lift stall, expressed in non-dimensional time, and the presence of 18 empirical coefficients, 6 each $(r_{j0}, r_{j2}, a_{j0}, a_{j2}, E_{j2})$ associated with lift $(j = l)$, moment $(j = m)$, and drag $(j = d)$. The coefficients are

$$r_j = (r_{j0} + r_{j2}.\Delta C_L^2)^2 \tag{9}$$

$$a_j = a_{j0} + a_{j2}.\Delta C_L^2 \tag{10}$$

$$E_j = E_{j2}.\Delta C_L^2 \tag{11}$$

The quantity ΔC_L is called a measure of stall and can attain two possible values:

$$\Delta C_L = 0 \tag{12}$$

$$\Delta C_L = (p_0 - p_1)(\alpha - \alpha_f)p_c[e^{p_h(\alpha-\alpha_{cr})} - 1] \quad (13)$$

The separation criterion is based on the angle of attack, and three possible cases can occur. Case 1: if $\alpha < \alpha_{cr} = 15^o(1-M^2)$, ΔC_L is given by Eq. (12). Case 2: assume that at time $t = t_0$, $\alpha = \alpha_{cr}, \dot{\alpha} > 0$; then, at time $t > t_0 + \Delta t$, ΔC_L is given by Eq. (13). As ΔC_L is different from zero, separated flow loads become substantial. Case 3: when $\alpha < \alpha_{cr}$, ΔC_L is set to zero again (Eq. (12)) and the separated flow loads quickly decrease to zero.

Combined Aerodynamic Model. The complete aerodynamic model used in this study consists of the RFA model for attached flow loads, using a free wake model in order to obtain the non-uniform inflow. The ONERA dynamic stall model is used for separated flow loads. Thus the complete aerodynamic state vector for each blade section consists of RFA attached flow states and ONERA separated flow states, together with the representation of the free wake.

Method of Solution

The blade is discretized [2] using the global Galerkin method, based upon the free vibration modes of the rotating blade. Three flapping modes, two lead-lag modes and two torsional modes are used in the actual implementation. The combined structural and aerodynamic equations form a system of coupled differential equations than can be cast in state variable form. They are then integrated in the time domain using the Adams-Bashfort DE/STEP predictor-corrector algorithm. The trim procedure [17] enforces three force equilibrium equations (longitudinal, vertical and lateral forces) and three moment equilibrium equations (roll, pitch and yaw moments). A simplified tail rotor model is used, using uniform inflow and blade element theory. The six trim variables are the rotor shaft angle α_R, the collective pitch θ_0, the cyclic pitch θ_{1s} and θ_{1c}, the tail rotor constant pitch θ_t and the lateral roll angle ϕ_R. The trim procedure is based on the minimization of the sum J_R of the squares of trim residuals. At high advance ratios ($0.30 < \mu \leq 0.35$) in the presence of dynamic stall, an autopilot procedure described in Ref. 26 is used to accelerate convergence to the trim state. At higher advance ratios ($0.35 < \mu$), an iterative optimization program based on Powell's method is used to find the trim variables that minimize J_R.

Control Algorithm

This section presents a brief description of the control strategies that are employed in this aeroelastic simulation study of vibration reduction. Two different implementations of active control configurations are studied: (a) a single, actively controlled partial span trailing edge flap; and (b) a dual flap configuration, shown in Fig. 5, in which each flap is independently controlled. In each case, the controller will act to reduce the 4/rev vibratory hub shears and moments.

The control strategy is based on the minimization of a performance index described in [1–5, 27] that is a quadratic function of the vibration magnitudes $\mathbf{z}_i$ and control input amplitudes $\mathbf{u}_i$:

$$J = \mathbf{z}_i^T \mathbf{W_z} \mathbf{z}_i + \mathbf{u}_i^T \mathbf{W_u} \mathbf{u}_i, \quad (14)$$

The subscript i refers to the i-th control step, reflecting the discrete-time nature of the control. The time interval between each control step must be long enough to allow the system to return to the steady state so that the 4/rev vibratory magnitudes can be accurately measured. The matrices $\mathbf{W_z}$ and $\mathbf{W_u}$ are weighting matrices on the vibration magnitude and control input, respectively.

Conventional Control Approach (CCA). A linear, quasistatic, frequency domain representation of the vibratory response to control inputs is used [2, 3, 17]. The input harmonics are related to the vibration magnitudes through a transfer matrix $\mathbf{T}$, given by

$$\mathbf{T} = \frac{\partial \mathbf{z_i}}{\partial \mathbf{u_i}}. \quad (15)$$

The optimal control is:

$$\mathbf{u}_i^* = -\mathbf{D}^{-1}\mathbf{T}^T\{\mathbf{W_z}\mathbf{z}_{i-1} - \mathbf{W_z}\mathbf{T}\mathbf{u}_{i-1}\}, \quad (16)$$

where

$$\mathbf{D} = \mathbf{T}^T\mathbf{W_z}\mathbf{T} + \mathbf{W_u} \quad (17)$$

Control in Presence of Flap Deflection Saturation

In the practical implementation of the ACF, adaptive materials based actuation, using piezoelectric or magnetostrictive materials, has been extensively studied. Adaptive materials are limited in their force and stroke producing capability, leading to fairly small angular deflections. From a control perspective this leads to saturation which introduces serious problems for vibration control. This important problem was studied and solved effectively in

a recent paper by Cribbs and Friedmann [28]. This approach to dealing with saturation, described below, is also used in this paper. Saturation is treated by the auto weight approach [28]. The weighting matrix $\mathbf{W_u}$ is represented in a form which allows its modification by premultiplying it by a scalar c_{wu} that is continuously adjusted. The controller manipulates the scalar multiplier to provide the proper flap constraints. If the flap deflection is overconstrained, the controller reduces the value of c_{wu} and a new optimal control is calculated. If the flap deflection is underconstrained, the controller increases the value of c_{wu} and a new optimal control is calculated. The iterative procedure reduces or increases c_{wu} until the optimal control converges to the desired deflection limits within a prescribed tolerance.

Incorporation of Freeplay into the Model

The effect of incorporating a freeplay type of nonlinearity, consisting of a spring freeplay combination depicted in Figs. 1 and 2 into the analysis is described next. Hinge moment equilibrium is enforced at the flap hinge. Thus, the flap can be considered to be a free flap, when an additional restoring moment is added to the hinge moment equilibrium equation. For $|\delta_f - \delta_p| \leq \delta_a$, the spring constant is set to zero, and for $|\delta_f - \delta_p| \geq \delta_a$, it has a finite value K_δ. It is assumed that the freeplay angle δ_a is constant when a control input δ_p is applied to the flap.

The implementation of the freeplay nonlinearity follows the free flap model used by Myrtle [29]. The flap deflection δ_f is considered an unknown quantity, and the flap degree of freedom is added to the blade degrees of freedom. Thus, the total number of structural dynamic degrees of freedom is given by:

$$\mathbf{q_b} = \left[\begin{array}{cccccccc} q_{w1} & q_{w2} & q_{w3} & q_{v1} & q_{v2} & q_{\phi 1} & q_{\phi 2} & \delta_f \end{array} \right]^T . \tag{18}$$

Since the flap is free, the hinge moment is zero. The hinge moment consists of contributions due to inertial, gravitational and aerodynamic loads:

$$H_{m_I}(\mathbf{q_b}) + H_{m_G}(\mathbf{q_b}) + H_{m_A}(\mathbf{q_b}) = 0. \tag{19}$$

A linear torsional spring is incorporated by adding a hinge moment due to the hinge stiffness as depicted on Figs. 1 and 2, the positive direction of flap deflection is shown on Fig. 1:

$$H_{m_I}(\mathbf{q_b}) + H_{m_G}(\mathbf{q_b}) + H_{m_A}(\mathbf{q_b}) = 0 \quad when \quad |\delta_f - \delta_p| \leq \delta_a \tag{20}$$

$$H_{m_I}(\mathbf{q_b}) + H_{m_G}(\mathbf{q_b}) + H_{m_A}(\mathbf{q_b}) - K_\delta \delta_e = 0 \quad when \quad |\delta_f - \delta_p| \geq \delta_a \tag{21}$$

where δ_e, shown in Fig. 2, is given by:

$$\delta_e = \delta_f - \delta_p - \delta_a \quad when \quad \delta_f \geq \delta_p + \delta_a \tag{22}$$

$$\delta_e = \delta_f - \delta_p + \delta_a \quad when \quad \delta_f \leq \delta_p - \delta_a \tag{23}$$

An approximate representative value for the spring constant associated with a typical actuation system has been estimated using the X-Frame piezoelectric actuator described in Ref. 30. Assuming that the control rod ARB-3 can undergo elastic deformations and using the description and dimensions provided in pages 48 and 270 of Ref. 30, the following approximate spring constant has been obtained:

$$K_\delta = 1.296.10^4 N.m/rad. \tag{24}$$

To validate the model, the freeplay angle δ_a is assumed first to be zero, and the calculations are carried out for a typical helicopter configuration for which the overall properties are specified in the Results section. When K_δ is large, Eq. (21) mandates a small value for δ_e. Results obtained using a prescribed flap deflection (for which K_δ is infinite) are compared with results for a large, but finite, value of K_δ ($K_\delta = 2.10^6 N.m/rad$), when the freeplay angle is set to zero.

The baseline vibratory hub shears and moments obtained using different values of flap spring stiffness, K_δ, are shown in Fig. 6. For each vibratory hub shear or moment, the left most bar represents the case when the flap deflection is prescribed and the elastic flap deflection is zero (i. e. $K_\delta \to 0$). The next adjacent bar (to the right) represents the vibratory loading obtained with a large, but finite, value of K_δ. The vertical hub shear is changed by 30% and all other hub shears and moments change by less than 5%. To determine the reason for this discrepancy, the flap deflections obtained for this case were Fourier-transformed and the results are depicted in Fig. 7. The lower harmonics of flap deflection (up to 7/rev) as well as some higher harmonics, 1006/rev and 1007/rev, are significant, while all others are very small. The same data, limited to frequencies lower than 10/rev, is displayed again for the sake of clarity in Fig. 8. Lower harmonics of flap deflection (up to 7/rev) as well as some higher harmonics, 1006/rev and 1007/rev, are significant, and all other components are very small. The high-frequency peak is equal to the fundamental frequency of the spring used in the model for freeplay shown in Fig. 1.

In order to identify which flap deflection harmonics are responsible for the vertical hub shear change the results obtained, when only some harmonics of

the flap deflection are retained, are also presented in Fig. 6. For each vibratory hub shear or moment, the third bar (from the left) represents the value obtained when the flap deflection is prescribed as follows: all harmonics of the flap deflection are set to zero, except its constant part, and the 1-7/rev, 1006/rev and 1007/rev harmonics, and the nonzero components have their values presented in Fig. 7. The vibratory hub shears and moments are within 5% of their counterparts when no flap deflection harmonics are neglected, as evident from comparing the second and third bars (from left). Therefore, the 30% vertical hub shear change is caused by the nonzero harmonics of flap deflection. The fourth bar (from left) represents the vibratory hub shears and moments obtained when the 1006/rev and 1007/rev are also set to zero. The vibratory hub shears and moments are similar to their counterparts when the flap deflection is set to zero, as evident from comparing the first and fourth bars (from left). Therefore, the 1006/rev and 1007/rev flap deflection harmonics, associated with the spring model, are responsible for the change in vibratory loads. The fifth bar represents results when all flap deflection harmonics except these two are neglected: the hub shears and moments are within 5% of the results obtained when K_δ takes a finite value. This confirms the certral role of the 1006/rev and 1007/rev flap deflection harmonics in the change in vibratory loads.

Figure 9 depicts the flap deflections corresponding to the case for which the vibratory hub shears and moments were shown in Fig. 6. The difference in vertical hub shear is caused by small deflections, less than 2.10^{-5} degrees, associated with larger harmonics. However, the large values of the second derivatives of the higher flap deflection harmonics change the inertia loading and therefore the vibratory loads. The hinge moments for the cases shown in Fig. 9 are depicted in Fig. 10. A comparison of the curves show that the 1006-1007/rev harmonics of the flap deflection do not have a large effect on hinge moment equilibrium. The principal equilibrium is satisfied by the lower harmonics (up to 7/rev) of the flap deflection, with little effect on vibratory hub shears and moments. Therefore, the higher flap deflection harmonics (1006/rev, 1007/rev) make only a negligible contribution towards satisfying the hinge moment equilibrium. In conclusion, the spring model has been validated, because the discrepancies between the results obtained for the prescribed flap condition and those for the case of large spring stiffness have been explained in a satisfactory manner.

Results

The helicopter configuration used in this study resembles approximately a MBB BO-105 four-bladed hingeless rotor. The data used in the computations is summarized in Table 1. The characteristics of the single and dual flap configurations are shown on Table 2. In Table 2, superscripts 1 and 2 indicate the outboard and inboard flaps, respectively, for the dual flap configuration. The portion of the blade spanned by the single flap is equal to the sum of the span covered by the dual flap configuration, as shown in Fig. 5.

Vibration reduction in the presence of dynamic stall, at high advance ratios, is considered first. For this case the vibration reduction capability of both single and dual flap configurations is examined. The vibration reduction capabilities of the two flap configurations are shown on Fig. 11. The single flap achieves a 40% reduction in vertical hub shear, but all other vibratory loads are reduced by 70-85%. The dual flap configuration reduces all loads by 70-95% and is at least 40% more effective than the single flap approach. This comparison shows the superiority of the dual flap configuration over the single flap, when dealing with alleviation of dynamic stall induced vibrations. Excellent vibration reduction in presence of dynamic stall is achieved by this configuration. This reduction is much better than what has been documented in the literature before [13].

Figure 12 depicts the dynamic stall locus, as defined by flow separation and reattachment, without control (diamonds) and with control (squares). The dynamic stall termination changes little in the presence of control (the difference in azimuth does not exceed 2^o), however the onset of dynamic stall has been significanlty altered. The boundaries of the dynamic stall zone is reduced by 30% from a region that extends between $240^o \leq \psi \leq 290^o$ to a region that is much narrower $255^o \leq \psi \leq 290^o$. This provides an indication about the mechanism of vibration reduction by active control. However, it should be noted that the figure is for a blade without pretwist and not a very high advance ratio.

The optimal flap deflection required for the vibration reduction in the single flap configuration is shown on Fig. 13. The maximum flap amplitudes are about 15^o. Figure 14 displays the flap deflections for the dual flap configuration; here again, the maximum deflection of both flaps is about 15^o. However, actuator technologies based on smart materials severely limit flap deflections to a maximum of 5^o. Furthermore, flap deflections of 15^o are not acceptable from a practical implementation point of view.

Therefore, additional results taking into account actuator saturation that allows practical limits on flap deflections have been obtained. The maximum allowable flap deflection for the cases considered here was set to 4^o, which is the value considered in an earlier study [28]. Saturation limits are imposed using the approach described in a previous section. Results for vibration reduction are presented in Fig. 15 for the single and dual flap configurations. The vertical hub shear is unchanged, but vibratory hub shear reduction is not affected by saturation; reductions of 70-80% are obtained again. However, vibratory hub moments are reduced 60-85% instead of 80-90%.

These results indicate that vibration reduction with the single flap configuration operating with and without saturation limits is similar. However, the flap operating without saturation limits reduces vibratory hub loads by an additional 10-30% when compared to the saturated flaps. These results are consistent with the observation made in an earlier paper [28] where the effects of dynamic stall were not included.

The flap deflections with and without saturation for the single flap configuration are shown on Fig. 16. The maximum allowed flap deflections occurs at $\psi = 225^o$, that is just before a large portion of the blade enters dynamic stall. This result confirms that the main feature of the control is to postpone dynamic stall entry, shown in Fig. 12. When saturation is not taken into account, flap deflections are unconstrained, and large deflections can occur while producing only a small amount of vibration alleviation. This appears to be the case on the advancing portion part of the rotor disk.

The influence of pretwist on the vibration alleviation capability of the actively controlled flap is considered next. The baseline and controlled vibratory hub shears and moments are presented in Fig. 17, when the pretwist angle is a linear function of r, with $\theta_{pt} = 0^o$ at the root and $\theta_{pt} = -8^o$ at the tip of the blade. The baseline vibrations are smaller (between 25% and 50%) than their counterparts without pretwist. The controlled vertical hub shear displays a 40% reduction with respect to the baseline, which is similar to the vertical hub reduction obtained without pretwist. The other vibratory hub shears and moments are reduced 50-60%. Figure 18 depicts the dynamic stall locus, as defined by flow separation and reattachment, without control (diamonds) and with control (squares). The dynamic stall area changes little in the presence of control. This is due to the large angles of attack (up to 19^o) at the root of the blade, due to the pretwist distribution.

The robustness of vibration alleviation using an actively controlled flap in the presence of freeplay is also examined. The baseline vibratory shears and moments, when the freeplay angle is allowed to have four different values between $0^o \leq \delta_a \leq 1.14^o$, are depicted in Fig. 19. The vibratory hub shears and moments do not change by more than 10% when the freeplay angle varies, however for $\delta_a = 1.14^o$, the vertical shears increases by 25%. The flap deflections for each value of the freeplay angle are shown in Fig. 20. The maximum flap deflection when $\delta_a = 0^o$ is less than 0.1^o. The two characteristics evident in Fig. 9, namely, small amplitude oscillations at the spring fundamental frequency and small frequency flap deflection history for hinge moment equilibrium, are visible again. Over most of the azimuth range, the values of the flap deflection are below $-\delta_a$.

Next, results in the presence of CCA optimal control are presented for the single flap configuration. The baseline and controlled vibratory hub shears and moments are presented in Fig. 21. The vertical hub shear is reduced at least by 40% for all values of δ_a considered. Therefore, the presence of freeplay does not jeopardize the effectiveness of the ACF as a vibration alleviation device. As the freeplay angle increases, however, there is a degradation in the reduction of the longitudinal hub shear and rolling and pitching hub moments. The flap deflections corresponding to the above vibration reduction results are represented in Fig. 22. The maximum flap deflection increases with the freeplay angle, from 6^o for $\delta_a = 0^o$ to 14^o for $\delta_a = 1.14^o$. All flap deflection histories display low flap deflections in the advancing blade region and large peaks over the retreating blade and dynamic stall region.

Vibration alleviation results obtained when saturation limits are imposed are presented in Fig. 23. The vertical hub shear is reduced by about 30% for all values of the freeplay angle. Therefore, even if the alleviation of other vibratory shears and moments is moderately degraded when the freeplay angle increases, the saturated ACF is an effective vibration alleviation device. The flap deflections associated with this vibration reduction are depicted in Fig. 24. The flap deflection histories are similar, and large peaks before and after the dynamic stall region are reproduced for all values of the freeplay angle.

Conclusions

A fairly extensive numerical simulation of vibration reduction at high speed flight using actively controlled flaps has been conducted. The ONERA dynamic stall model was used for the representation of the unsteady aerodynamic loading in the separated flow region. Both single flap and dual flap configurations were studied, and limits on flap deflections were imposed. The principal conclusions obtained are provided below.

1. The ACF implemented either as a single flap or in the dual flap configuration is an effective means for alleviating the unfavorable effects due to dynamic stall.

2. The physical mechanism for reducing vibrations due to dynamic stall appears to be associated with delayed entry of the retreating blade into the stall region; combined with a reduction in the stall region over the area of the disk

3. The dual flap configuration appears to have an advantage over the single flap configuration in its ability to alleviate the undesirable effects associated with dynamic stall.

4. The actively controlled flap, implemented in either single or dual flap configurations, is more effective at alleviating dynamic stall effects than the HHC approach studied in Ref. 13. The primary reason for the effectiveness of ACF is due to the fact that it represents a local controller, that is inherently more suitable for dealing with local effects such as dynamic stall. The HHC approach affects the entire blade and thus is at a disadvantage when attempting to alleviate local effects.

5. Imposition of flap deflection limits, and the appropriate treatment of saturation play an important role in the ability of the ACF, in both configurations, to achieve alleviation of dynamic stall related effects. Therefore, a careful treatment of these issues is necessary for the practical implementation of the ACF in rotorcraft.

6. Pretwist distributions have a minor influence on the vibration alleviation effectiveness of the ACF.

7. Vibration alleviation is not jeopardized by the presence of freeplay type of nonlinearity. The vibratory hub shear reduction is not diminished by the introduction of freeplay, and a moderate degradation of the reduction of other vibratory hub shears and moments is noticed.

Acknowledgment

Partial support from the FXB Center for Rotary and Fixed Wing Air Vehicle Design, and DAAD Grant 19-02-1-0202 from ARO with Dr. G. Anderson as grant monitor are gratefully acknowledged.

References

[1] Friedmann, P. P. and Millot, T. A., "Vibration Reduction in Rotorcraft Using Active Control: A Comparison of Various Approaches," *Journal of Guidance, Control, and Dynamics*, Vol. 18, No. 4, 1995, pp. 664–673.

[2] Millott, T. A. and Friedmann, P. P., "Vibration Reduction in Helicopter Rotors Using an Actively Controlled Partial Span Trailing Edge Flap Located on the Blade," NASA CR-4611, 1994.

[3] Myrtle, T. F. and Friedmann, P. P., "Application of a New Compressible Time Domain Aerodynamic Model to Vibration Reduction in Helicopters Using an Actively Controlled Flap," *Journal of the American Helicopter Society*, No. 1, 2001, pp. 32–43.

[4] de Terlizzi, M. and Friedmann, P. P., "Active Control of BVI Induced Vibrations Using a Refined Aerodynamic Model and Experimental Correlation," *55th Annual Forum of the American Helicopter Society*, Montréal, Canada, May 1999, pp. 599–618.

[5] Friedmann, P. P., de Terlizzi, M. and Myrtle, T. F., "New Developments in Vibration Reduction with Actively Controlled Trailing Edge Flaps," *Mathematical and Computer Modeling*, Vol. 33, 2001, pp. 1055–1083.

[6] Straub, F. K., "Active Flap Control for Vibration Reduction and Performance Improvement," *Proceedings of the 51st American Helicopter Society Forum*, Fort Worth, Tex., May 1995, pp. 381–392.

[7] Straub, F. K. and Charles, B. D., "Comprehensive Modeling of Rotors with Trailing Edge Flaps," *Proceedings of the 55th Forum of the American Helicopter Society*, Montréal, Canada, May 1999.

[8] Chopra, I., Milgram, J. and Straub, F. K., "Comprehensive Rotorcraft Aeroelastic Analysis with Trailing Edge Flap Model," *Proceedings of the 52th Forum of the American Helicopter Society*, Washington, D. C., June 1996, pp. 715–725.

[9] Friedmann, P. P., "Rotary-Wing Aeroelasticity - Current Status and Future Trends," *Proceedings of the 39th AIAA Aerospace Sciences Meeting and Exhibit*, AIAA Paper No. 2001-0427, Reno, Nev., January 2001.

[10] Shin, S. J. and Cesnik, C. E. S., "Forward Flight Response of the Active Twist Rotor for Helicopter Vibration Reduction," *Proceedings of the 42th AIAA/ASME/ASCE/AHS/ACS Structures, Structural Dynamics and Materials Conference*, AIAA Paper No. 2001-1357, Seattle, Wash., April 2001.

[11] Wilbur, M. L., Mirick, P. H., Yeager, W. T., Langston, C. W., Shin, S. J., and Cesnik, C. E. S., "Vibratory Loads Reduction Testing of the NASA/Army/MIT Active Twist Rotor," *Proceedings of the American Helicopter Society 57th Annual Forum*, Washington, D. C., May 2001.

[12] Leishman, J. G., *Principles of Helicopter Aerodynamics*, Cambridge University Press, Cambridge, 2000.

[13] Nguyen, K., "Active Control of Helicopter Blade Stall," *AIAA Dynamics Specialists Conference*, AIAA Paper No. 96-1221, Salt Lake City, Utah, April 1996.

[14] Petot, D., "Differential Equation Modeling of Dynamic Stall," *La Recherche Aérospatiale*, Vol. 5, 1989, pp. 59–71.

[15] Leishman, J. G. and Beddoes, T. S., "A Semi-Empirical Model for Dynamic Stall," *Journal of the American Helicopter Society*, , No. 4, 1989, pp. 3–17.

[16] Fulton, M. and Ormiston, R. A., "Small-Scale Rotor Experiments with On-Blade Elevons to Reduce Blade Vibratory Loads in Forward Flight," *Proceedings of the 54th Annual Forum of the American Helicopter Society*, Washington, D. C., May 1998, pp. 433–451.

[17] de Terlizzi, M., *Blade Vortex Interaction and its Alleviation Using Passive and Active Control Approaches*, Ph.D. thesis, University of California, Los Angeles, 1999.

[18] Depailler, G. and Friedmann, P. P., "Alleviation of Dynamic Stall Induced Vibrations Using Actively Controlled Flaps," *Proceedings of the 58th Forum of the American Helicopter Society*, Montréal, Canada, June 2002.

[19] Tang, D. M. and Dowell, E. H., "Flutter and stall response of a helicopter blade with structural nonlinearity," *Journal of Aircraft*, Vol. 29, 1992, pp. 953–960.

[20] Brase, L. O. and Eversman, W., "Application of Transient Aerodynamics to the Structural Nonlinear Flutter Problem," *Journal of Aircraft*, Vol. 25, No. 11, 1988, pp. 1060–1068.

[21] Johnson, W., *A Comprehensive Analytical Model of Rotorcraft Aerodynamics and Dynamics, Vol. I: Theory Manual*, Johnson Aeronautics, Palo Alto, CA, 1988.

[22] McCormick, B. W., *Aerodynamics of V/STOL Flight*, Academic Press, New York, 1967.

[23] Wenzinger, C. J. and Harris, T. A., "Wind-Tunnel Investigation of a NACA 23012 Airfoil with Various Arrangements of Slotted Flaps," NACA Report 664, 1939.

[24] Depailler, G. and Friedmann, P. P., "Reduction of Vibrations due to Dynamic Stall in Helicopters using an Actively Controlled Flap," *Proceedings of the 43rd AIAA/ASME/ASCE/AHS/ACS Structures, Structural Dynamics and Materials Conference*, AIAA Paper No. 2002-1431, Denver, Colo., April 2002.

[25] Peters, D. A., "Toward a Unified Lift Model for Use in Rotor Blade Stability Analyses," *Proceedings of the 40th Forum of the American Helicopter Society*, Arlington, Va., May 1984.

[26] Peters, D. A., Bayly, P. and Li, S., "A Hybrid Periodic-Shooting, Autopilot Method for Rotorcraft Trim Analysis," *Proceedings of the 52th Forum of the American Helicopter Society*, Washington, D.C., June 1996, pp. 780–792.

[27] Johnson, W., "Self-Tuning Regulators for Multicyclic Control of Helicopter Vibration," NASA TP-1996, 1982.

[28] Cribbs, R. and Friedmann, P. P., "Actuator Saturation and its Influence on Vibration Reduction by Actively Controlled Flaps," *Proceedings of the 42nd*

AIAA/ASME/ASCE/AHS/ACS Structures, Structural Dynamics and Materials Conference, AIAA Paper No. 2001-1467, Seattle, Wash., April 2001.

[29] Myrtle, T. F., *Development of an Improved Aeroelastic Model for the Investigation of Vibration Reduction in Helicopter Rotors Using Trailing Edge Flaps*, Ph.D. thesis, University of California, Los Angeles, 1998.

[30] Prechtl, E. F., *Design and Implementation of a Piezoelectric Servo-Flap Actuation System for Helicopter Rotor Individual Blade Control*, Ph.D. thesis, Massachusetts Institute of Technology, 2000.

Table 1: Elastic blade configuration

Rotor Data	
$N_b = 4$	$c_b = 0.05498 L_b$
$\omega_{F1} = 1.123$	$C_{do} = 0.01$
$\omega_{L1} = 0.732$	$C_{mo} = 0.0$
$\omega_{T1} = 3.17$	$a_o = 2\pi$
$\gamma = 5.5$	$\sigma = 0.07$
Helicopter Data	
$C_W = 0.00515$	
$X_{FA} = 0.0$	$Z_{FA} = 0.3$
$X_{FC} = 0.0$	$Z_{FC} = 0.3$

Table 2: Flap configurations

$c_{cs} = 0.25 c_b$	
Single Flap	
$x_{cs} = 0.75 L_b$	$L_{cs} = 0.12 L_b$
Dual Flap	
$x^1_{cs} = 0.72 L_b$	$L^1_{cs} = 0.06 L_b$
$x^2_{cs} = 0.92 L_b$	$L^2_{cs} = 0.06 L_b$

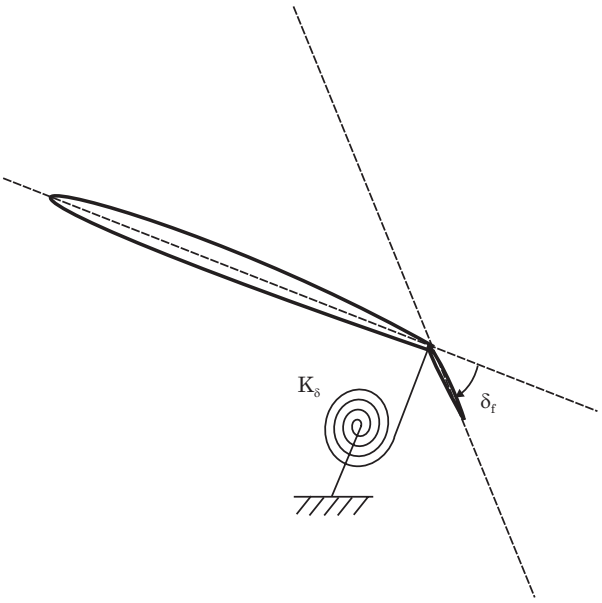

Figure 1: Model for the torsional spring constraint acting on the flap.

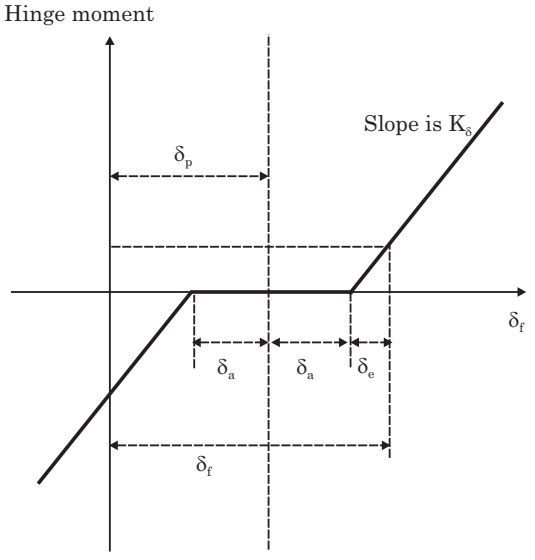

Figure 2: Hinge moment as a function of flap deflection.

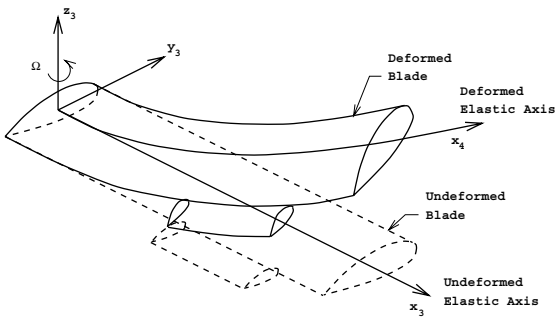

Figure 3: Schematic representation of the undeformed and deformed blade/actively controlled flap configuration.

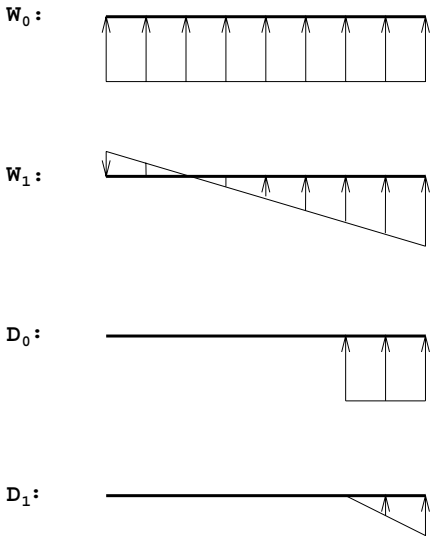

Figure 4: Normal velocity distributions corresponding to generalized airfoil and flap motions W_0, W_1, D_0, and D_1.

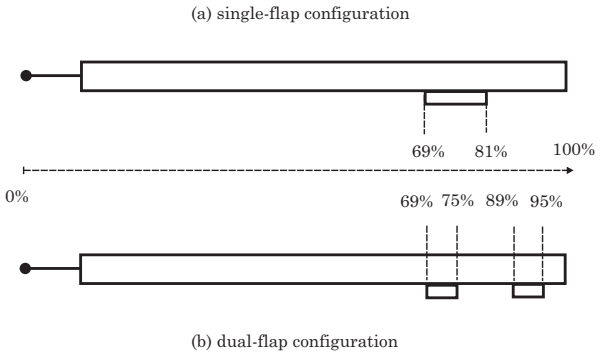

Figure 5: Single and dual flap configurations.

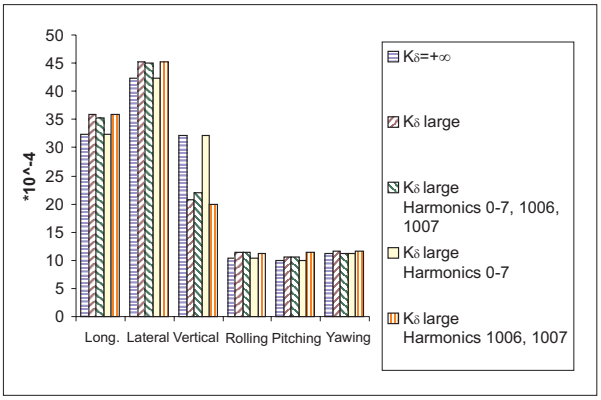

Figure 6: Baseline vibrations for prescribed flap deflections ($K_\delta = +\infty$) and for a large value of K_δ; δ_a=0; and μ=0.35.

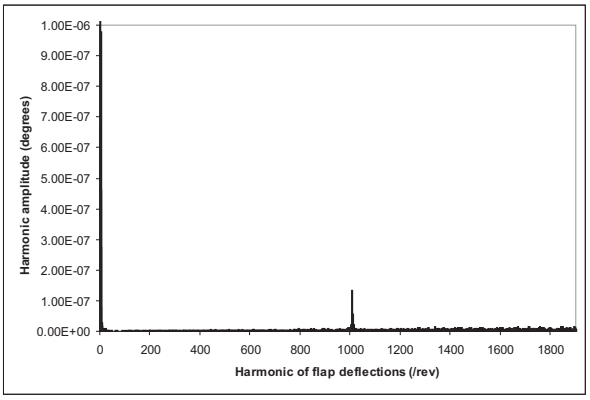

Figure 7: Fourier analysis of the flap deflection δ_f for a large value of K_δ; δ_a=0; and μ=0.35. Frequencies are in per rev.

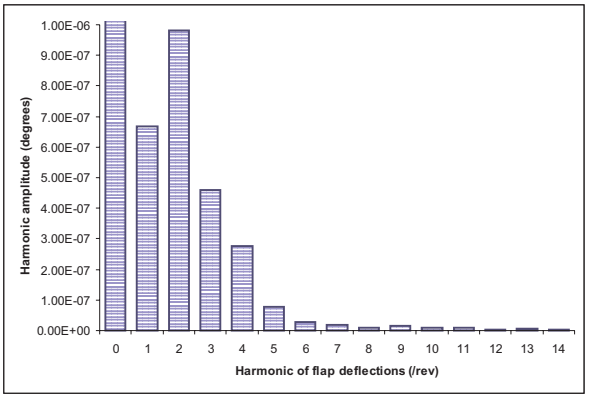

Figure 8: Fourier analysis, limited to lower frequencies, of the flap deflection δ_f for a large value of K_δ; δ_a=0; and μ=0.35. Frequencies are in /rev.

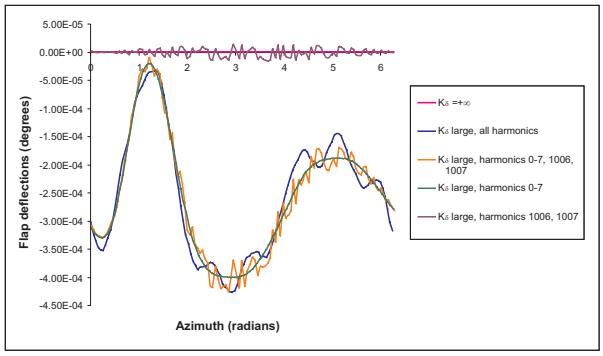

Figure 9: Flap deflections, degrees, for prescribed flap deflections ($K_\delta = +\infty$) and for a large value of K_δ; δ_a=0; and μ=0.35.

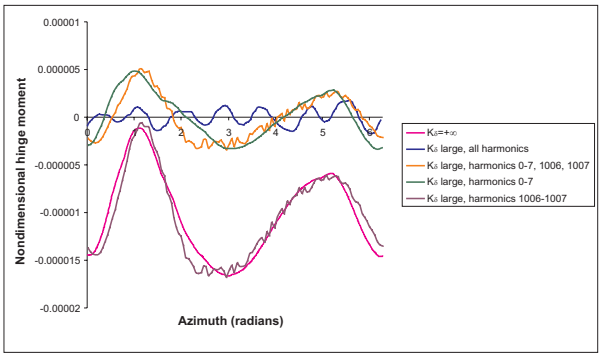

Figure 10: Flap hinge moment for prescribed flap deflections ($K_\delta = +\infty$) and for a large value of K_δ; δ_a=0; and μ=0.35.

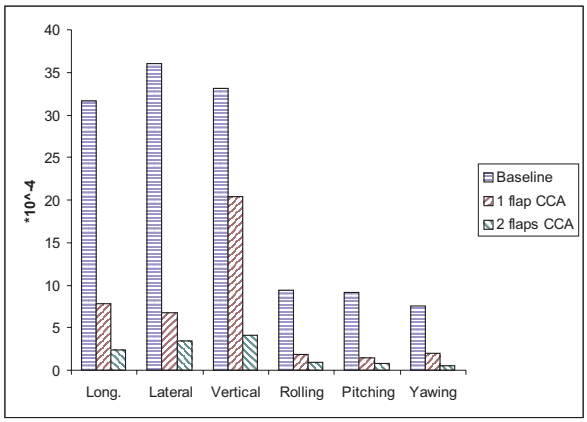

Figure 11: Vibration reduction, CCA, μ=0.35.

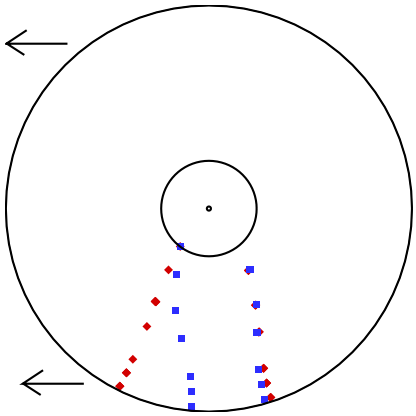

Figure 12: Dynamic stall locus control (squares) and no control (diamonds), μ=0.30. The center of the figure represents the hub region, the outer circle depicts the rotor disk and the arrows show the direction of forward flight. Aerodynamic loads are neglected in the inner circle.

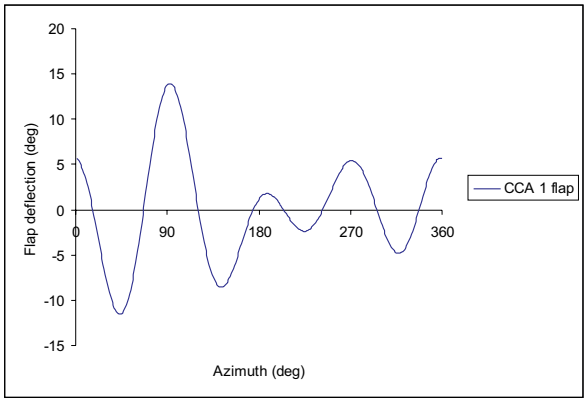

Figure 13: Flap deflections, CCA, single flap configuration, μ=0.35.

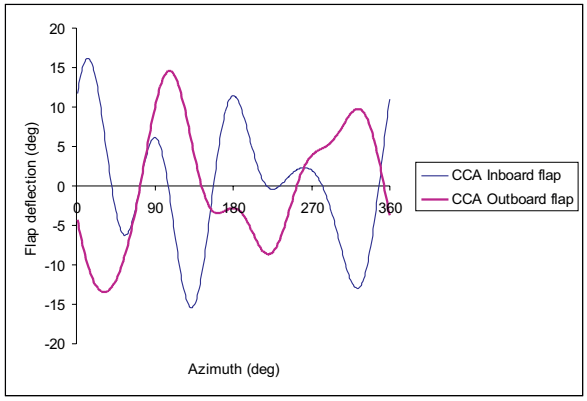

Figure 14: Flap deflections for dual flap configuration, CCA, μ=0.35.

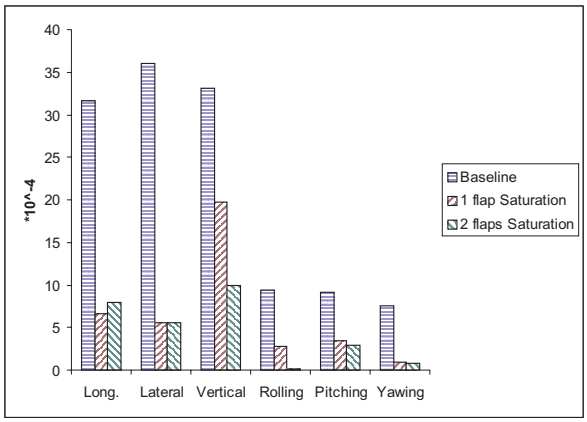

Figure 15: Vibration reduction with saturation limits, μ=0.35.

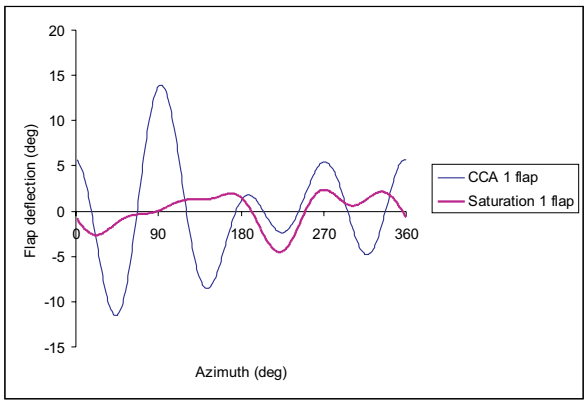

Figure 16: Flap deflections, effect of saturation, μ=0.35.

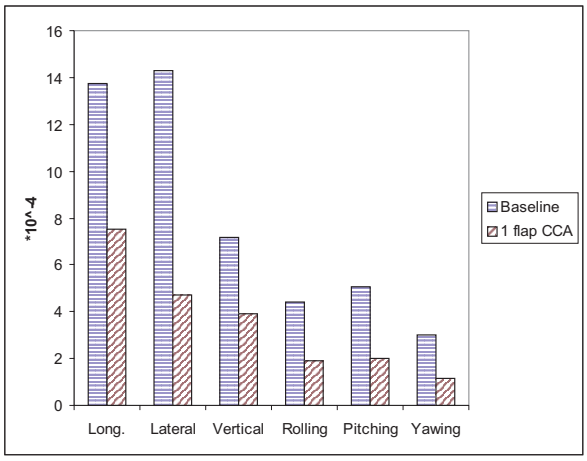

Figure 17: Vibration reduction, CCA, pretwist, μ=0.35.

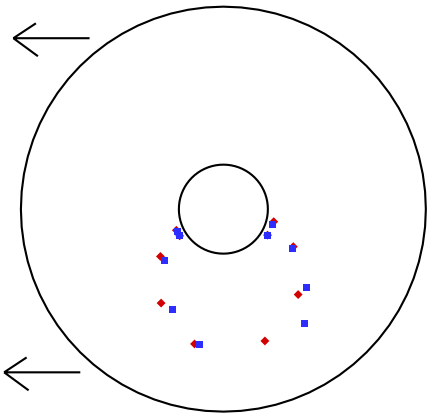

Figure 18: Dynamic stall locus control (squares) and no control (diamonds), pretwist, μ=0.30. The center of the figure represents the hub region, the outer circle depicts the rotor disk and the arrows show the direction of forward flight. Aerodynamic loads are neglected in the inner circle.

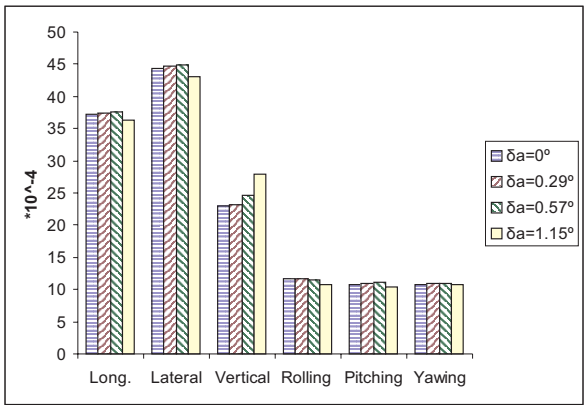

Figure 19: Baseline vibrations for different values of the freeplay angle, μ=0.35.

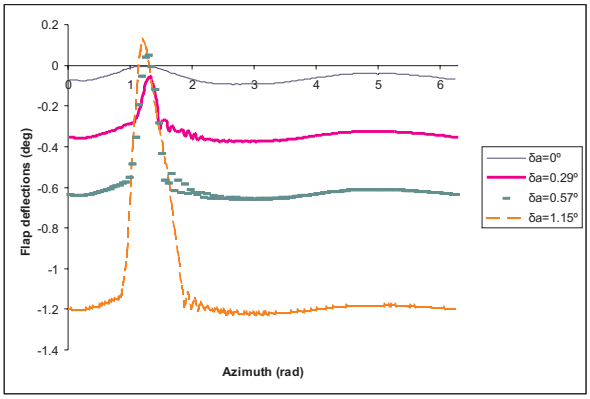

Figure 20: Baseline flap deflections for different values of the freeplay angle, μ=0.35, and without control.

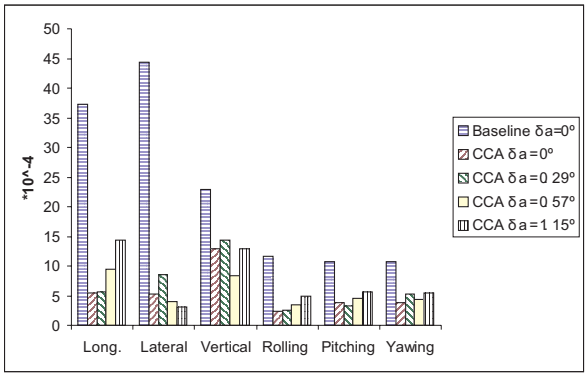

Figure 21: Vibration reduction, CCA, for different values of the freeplay angle, μ=0.35, single flap configuration.

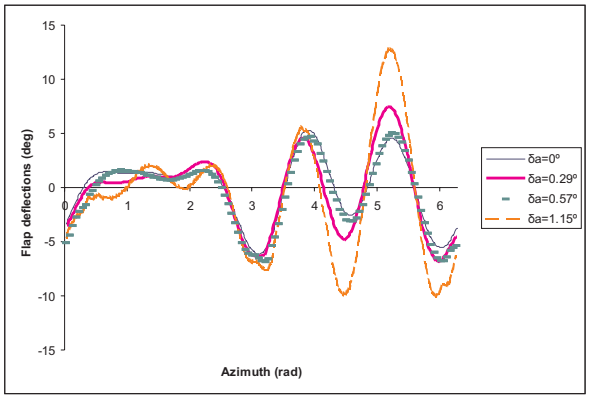

Figure 22: Flap deflections, CCA, for different values of the freeplay angle, μ=0.35.

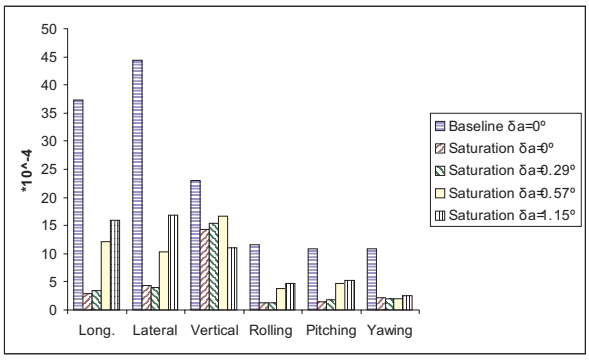

Figure 23: Vibration reduction, saturation, for different values of the freeplay angle, μ=0.35, single flap configuration.

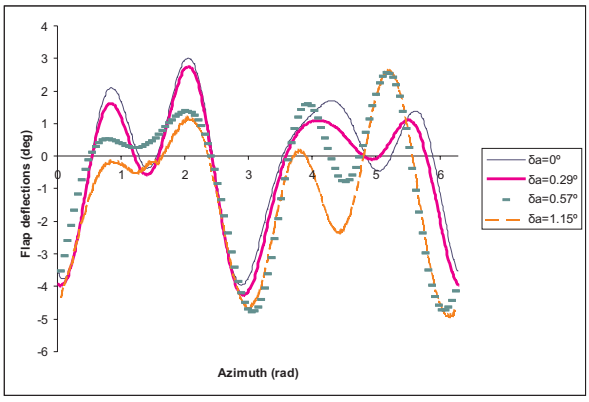

Figure 24: Flap deflections, saturation, for different values of the freeplay angle, μ=0.35.